Evaluating candidate materials for balance of plant components in SOFC: Oxidation and Cr evaporation properties

N.B. When citing this work, cite the original published paper.

(article starts on next page)

Contents lists available at ScienceDirect

Corrosion Science

Evaluating candidate materials for balance of plant components in SOFC: Oxidation and Cr evaporation properties

Mareddy Jayanth Reddy *, Jan-Erik Svensson , Jan Froitzheim

Chalmers University of Technology, Department of Chemistry and Chemical Engineering, Division of Energy and Materials, Kemivägen 10, SE-412 96, Gothenburg, Sweden

ARTICLE INFO

ABSTRACT

Balance of plant (BOP) components made of metallic materials in solid oxide fuel cells are subject to high-temperature corrosion and are a significant source of volatile chromium species. Prospective Fe and Ni-base alloys, AISI 441, AISI 444, a FeCrAl alloy A197/Kanthal® EF101, alloy 600, and alloy 800H are investigated for their suitability to BOP components. Oxidation kinetics and chromium evaporation were employed to study the selected alloys at 650 °C and 850 °C for 500 h. A197 performed the best while AISI 441 and AISI 444, performed the worst. Pre-oxidation significantly improved the performance of the alloys at 650 ºC.

1. Introduction

The global consumption of energy is increasing rapidly, and so are CO_2 emissions, which are widely regarded as the primary cause of global warming. Alternative energy conversion devices with lower CO_2 emissions are necessary to meet the demand in energy consumption. Solid Oxide Fuel Cells (SOFC) have long been regarded as an attractive choice for future energy needs. The SOFC is a high-temperature electrochemical device that converts chemical energy in a fuel into electrical energy. SOFCs are promising because of their high electrical efficiency (up to 70 % [1]), fuel flexibility, low emissions, and silent operation. SOFC-based combined heat and power (CHP) can reach an efficiency as high as 90 % [2] and fulfil electrical and heating needs.

SOFCs provide high efficiency at all capacities, allowing them to scale in diverse fields such as automotive applications, residential applications, industrial applications, and centralized power production [3]. Despite these advantages, commercial success has been limited by high material costs and a short lifespan. Operating temperatures have been substantially reduced with recent developments in materials and manufacturing, allowing the widespread use of steel in the SOFC system. Steels are mainly used as interconnects, and most research has focused on chromia-forming ferritic grades due to the moderate conductivity of the chromia scale, ease of manufacturing, and coefficients of thermal expansion (CTE) similar to those of the ceramics used in the cell.

However, the chromia-forming ferritic steels used for the interconnects have two significant drawbacks. The gradual growth of the

oxide layer during SOFC operating conditions leads to increased resistance across the cell, decreasing cell efficiency. The Cr_2O_3 scale also reacts with oxygen in the presence of water vapour at high temperatures to form volatile $CrO_2(OH)_2$. The reaction is shown in Eq. 1.

$$\frac{1}{2} \, Cr_2O_3 \, (s) + H_2O + \frac{3}{4} \, O_2 \rightarrow CrO_2(OH)_2 \, (g) \tag{1}$$
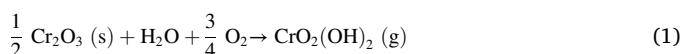
Chromium evaporation is dependent on various operating variables such as humidity, temperature, and oxygen partial pressure. Chromium evaporation reduces the lifetime of steel components and is also a significant issue for the oxygen transport membranes in SOFCs. The volatile Cr (VI) species react with the air electrode and are deposited on triple-phase boundaries. These deposits block the electrochemical oxygen reduction reaction, a phenomenon called chromium poisoning [4]. Chromium poisoning drastically reduces the efficiency and lifespan of the SOFCs. Applying protective coatings is known to minimise chromium evaporation and, in some cases, oxide growth [5–7].

Along with the interconnects, steels are widely used in the auxiliary components of a SOFC system, and these together are called the Balance Of Plant (BOP). BOP comprises the cell frame, cathode pre-heater, heat exchangers, thermal management equipment, pipework, pumps, fuel processors, control systems, start-up heater, and power conditioner [8]. A cathodic pre-heater is used to preheat reactant gases, thus preventing thermal stresses from rapid temperature variations in ceramic stacks. Heat exchangers are used to recover high-quality heat energy from the exhaust gas. Therefore, large parts of BOP components are subjected to

severe high-temperature operating conditions. The conventional ceramics used in BOP [9] are being replaced with metallic materials owing to their better mechanical properties, lower cost, and ease of manufacturing; simultaneously, metallic materials reduce the cost and weight of a SOFC system, making them attractive for mobile applications.

BOP components located upstream of the cell can be a significant source of volatile chromium species often overlooked [10]. Unlike the interconnects, BOP components are exposed to various temperatures depending on their function, location, and contact with the exhaust. Few studies have explored the oxidation and chromium evaporation properties of BOP steels in SOFC conditions [11–13]. Moreover, the BOP components in a SOFC system comprise up to 75 % of the system manufacturing cost [8]. It is essential to understand the performance and cost-effectiveness of the steels used. Coatings used to circumvent the chromium evaporation, and high oxidation rate in interconnects are harder to implement for BOP components due to complex-shaped system parts. However, the material selection for BOP components has greater design freedom as there are no restrictions on the conductivity of the scale and fewer restrictions on the CTE. For this reason, alumina former, austenitic materials, and Ferritic Stainless Steels (FSS) have been explored for application in BOP systems.

Ferritic stainless steels have been extensively studied for application as interconnects [14]. High-volume FSSs, such as type 441, type 430, and type 444, are particularly relevant due to lower material costs. Grolig et al. [15] have examined the oxidation and chromium evaporation of type 441 and found unacceptably high chromium evaporation and oxidation at 850 °C without a protective coating. Chromium evaporation data at lower temperatures are limited for these types of steels [16]. Type 444 has been proposed for interconnect applications [17,18]. Type 444 steel has been reported to have better oxidation resistance [19], higher creep, and greater fatigue resistance [20] than type 441. Despite these properties, austenitic materials are usually preferred in most high-temperature applications due to their optimal combination of strength, creep resistance, and microstructural stability with excellent oxidation resistance [21]. So far, few publications have reported the chromium evaporation characteristics of these materials.

Alloy 800H is a Fe-based austenitic solid-solution alloy, an alternative to expensive nickel-based alloys used in severe service conditions. It is used broadly in nuclear applications, furnace components, electrical power generation, and heat exchangers [22,23]. Considerable resistance to carburization and metal dusting enables it to be used in petrochemical processing, steam reformers, pigtails, and headers in hydrogen production [24,25]. Hence, it is particularly interesting for the anode side components involving hydrocarbon fuels in the SOFC system. In contrast, Ni-based superalloys are more expensive, with excellent high-temperature strength and resistance to corrosion and fatigue [26, 27]. Increasing the Ni content in alloys improves cyclic oxidation resistance, creep performance, and oxidation resistance [28]. Alloy 600 is a Ni-based alloy widely used as a standard engineering material with excellent mechanical properties. The versatility of the alloy's properties makes it suitable for various applications from cryogenic temperatures to 1000 °C [29]. The alloy is typically used in high-temperature applications in the chemical, heat-treating, and aeronautical industries.

Alumina formers have excellent high-temperature corrosion characteristics due to the low defect concentration in alumina, which results in a slow-growing and protective oxide scale. The parabolic rate constant for alumina formers is approximately two orders lower than that for chromia formers [30]. Stanislowski et al. [31] have shown that the exterior alumina scale formed on AluChrom YHf at 800 °C had a 99.9 % decrease in chromium evaporation than a pure chromia scale. Although FeCrAl steels have extremely low chromium evaporation once an alumina scale has been formed, other factors such as creep strength and weldability are commonly considered drawbacks of FeCrAl steels [32]. Alumina formers are traditionally used between 900–1200 °C to form protective α-alumina scales [33]. FeCrAl steels also tend to form brittle

phases upon application at lower temperatures [34]. However, the brittle phase formation can be mitigated by using Cr, and Al-lean compositions, which might, in turn, limit the ability of these steels to form an alumina scale. Nonetheless, Eklund et al. [35] have reported alumina scale formation at 600 °C on a Cr, Al-lean alloy alloyed with 1–2 % Si. FeCrAl alloys are known to form transient alumina layers at lower temperatures [36,37]. Understanding the chromium retention capabilities of the transient alumina scale formed at lower temperatures is essential for the application of these alloys in BOP components.

To choose the appropriate materials for BOP components, comprehensive knowledge of the high-temperature oxidation behaviour and lifespan of the materials in relevant conditions is necessary. Another important factor is cost; the Ni-based alloy 600 is expected to be the most expensive material, followed by alloy 800H. The ferritic steels, AISI 441, AISI 444, and FeCrAl alloy are significantly cheaper based on their alloy chemistry; however, it is expected that the current lower production volume of the FeCrAl alloy will result in a somewhat higher price.

This study evaluates the oxidation and chromium evaporation properties of selected materials in typical SOFC conditions. Chemical and morphological analyses are presented to correlate oxidation conditions to the resulting oxide microstructure. Time-resolved mass gain and chromium evaporation were measured at 650 °C and 850 °C for 500 h; subsequently, the oxide scale was characterized. The influence of pre-oxidation at 900 °C on the chromium evaporation and oxidation behaviour of the steels exposed at 650 °C was studied and compared to as-received material.

2. Materials and methods

Five alloys from four groups of materials were selected for this study: two commercial chromia-forming ferritic steels (AISI 441, AISI 444 (K44 M, Aperam steels)); alumina-forming ferritic steel A197 (Kanthal® EF101); a Fe-base austenitic alloy (Alloy 800 H); and a Ni-base austenitic alloy (Alloy 600). The composition in weight % of the alloys is given in Table 1. AISI 444 and AISI 441 are chromia-forming ferritic steels with similar chemical compositions; AISI 444 has a slightly higher content of Cr and Nb. AISI 444 is also alloyed with 2 wt% Mo, which is absent in AISI 441. A197 is a Cr, Al-lean FeCrAl alloy with 3.7 wt% Al, 12 wt% Cr, and reactive elements (RE). Alloy 800H is high-alloyed austenitic steel with about 20 wt% Cr and 30 wt% Ni with alloying elements such as Al and Ti. Inconel 600 (alloy 600) is a nickel-based superalloy, austenitic steel with 16 wt% chromium and 8 wt% iron. All the alloys except A197 were received in steel sheets with a thickness of 0.5 mm. The steel sheets were further cut into 17 × 15 mm coupons and exposed in the reactor without any surface pre-treatment. A197 was received as a 2 mm thick sheet and was further cut into square coupons (15 × 15 × 2 mm), which were ground to 0.5 mm using SiC paper to a grit #1200 finish in the final step. All the coupons were degreased and cleaned with acetone and ethanol using an ultrasonic bath at room temperature before exposure. The coupons were weighed using an XP6 scale (Mettler Toledo).

The exposures were conducted in a horizontal quartz tube reactor with continuous airflow. The air was saturated with 3% H_2O to represent high humidity conditions. 3% H_2O in the air was achieved by passing the air through a heated water bath connected to a condenser set at 24.4 °C. The airflow was set at 6000 sml min^{-1}, which corresponds to 27 cm/s to achieve a flow-independent reaction regime in the reactor. In-situ chromium evaporation measurements were made using a denuder technique developed by Froitzheim et al. [38]. Downstream of the samples, the gas was passed through a quartz silica tube (denuder) coated on the inside with Na_2CO_3. Volatile chromium species react with Na_2CO_3, according to Eq. 2.

$$Na_2CO_3(s) + CrO_2(OH)_2(g) \rightarrow Na_2CrO_4(s) + H_2O(g) + CO_2(g) \qquad (2)$$
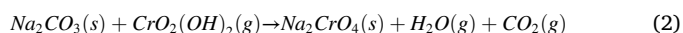
The denuders were exchanged at regular intervals without affecting the exposure. The removed denuders were leached with distilled water. The chromium species in the solution were quantified using an

Table 1
Chemical composition of the selected materials in wt%.

Material	DIN	C	Si	Mn	Cr	Ni	Ti	Al	Nb	Fe	Cu	Co	Mo
Alloy 800H	1.4958	0.07	0.4	0.6	20.8	30.4	0.3	0.28	–	Bal	0.24	–	–
Alloy 600	2.4816	0.02	0.18	0.24	16.25	74.19	0.29	0.22	0.08	7.93	0.35	0.06	–
A197	–	0.02	1.25	0.1	12.4	–	–	3.7	–	Bal	Reactive Elements		
AISI 444	1.4521	0.013	0.37	0.3	18.92	–	0.003	–	0.562	Bal	–	–	1.85
AISI 441	1.4509	0.02	0.58	0.42	17.53	0.28	0.164	0.0045	0.39	Bal	–	–	–

Evolution 60S Thermo Scientific spectrophotometer.

The exposures were conducted at 650 °C and 850 °C for 500 h. To understand the influence of pre-oxidation on mass gain and chromium evaporation, the coupons were pre-oxidized at 900 °C for 24 h in the air. These coupons were then exposed at 650 °C for 500 h. Three identical coupons were used per exposure, mounted on an alumina sample holder positioned parallel to the airflow. Two types of exposures were executed: discontinuous mass gain exposure, where the coupons were removed from the furnace at regular intervals after 24 h, 168 h, 336 h and 500 h to record mass, and isothermal chromium evaporation exposures, where the denuder was exchanged at regular intervals, allowing for time-resolved chromium evaporation.

The oxide scale of the exposed coupons was characterized with the use of XRD, SEM, EDX. The crystalline phases of the oxide scale were analysed using a Siemens D5000 powder diffractometer fitted with a grazing incidence beam. Cu-Kα radiation was used, and the incidence angle was set between 0.5−2° depending on the thickness of the oxide scale. The cross-sections were prepared using broad ion beam milling. The coupons were analysed using a JEOL JSM-7800 F Prime SEM equipped with an Oxford Instruments Energy Dispersive X-ray spectrometer (EDS).

3. Results

3.1. Gravimetric measurements

The isothermal oxidation kinetics, represented by discontinuous gravimetric measurements for the selected alloys exposed to air with 3 % H_2O at 650 °C and 850 °C, is presented in Fig. 1a and b, respectively. At 650 °C, alloy 800H, alloy 600, and A197 showed a net mass gain over time, while the alloys AISI 444 and AISI 441 showed net mass loss over time. Alloy 800H showed a much higher net mass gain (5.69 ± 0.31 mg/cm^2 after 500 h) than the other alloys at 650 °C, indicating inferior oxidation resistance. The mass gain of alloy 800H was especially fast

initially and stabilized after 168 h. The nickel-based alloy, alloy 600, showed a net mass gain of 0.342 ± 0.089 mg/cm^2 after 500 h. A197 showed the least positive net mass gain, 0.013 ± 0.0009 mg/cm^2, after 500 h. The steels AISI 444 and AISI 441 showed a similar net mass loss after 500 h; AISI 444 had a negative mass gain of -0.029 ± 0.005 mg/cm^2, and AISI 441 had a negative mass gain of -0.030 ± 0.003 mg/cm^2.

Both steels showed almost identical behaviour with an initial net mass gain after 24 h and a subsequent almost linear mass loss until 500 h. This behaviour, called paralinear oxidation, has been reported in the literature on similar alloys such as Crofer 22H [39] and Sanergy HT [39, 40] at 650 °C. The explanation for this is that the net mass gain is the sum of mass gain due to oxide scale formation and simultaneous loss due to chromium evaporation [39,41], as plotted in Fig. 1. During the first 24 h, the mass gain due to oxide scale growth was faster than mass loss caused by chromium evaporation, resulting in a positive net mass gain. However, as the oxide scale thickened, the oxidation rate dropped. In this region, the mass loss through chromium evaporation $CrO_2(OH)_2$ dominated, leading to net mass loss. Continuous chromium evaporation depletes the alloy from chromium. Chromium depletion can lead to the formation of less protective oxide scales, such as iron oxides leading to rapid oxidation, a phenomenon called breakaway oxidation [42].

All the selected alloys showed a net mass gain after 500 h at 850 °C. Alloy 800H again showed a fast initial mass gain (1.35 ± 0.075 mg/cm^2 after 24 h) followed by a slow mass gain for the rest of the exposure. After 500 h, the net mass gain was 1.52 ± 0.063 mg/cm^2, 4–5 times lower than the net mass gain at 650 °C. The reason for this will be discussed in Section 4.2. Alloy 600 showed a higher net mass gain than AISI 444 and AISI 441 in the first 24 h; however, the net mass gain of alloy 600 after 500 h was 0.38 ± 0.032 mg/cm^2, which was lower than that of AISI 444 and AISI 441. A197 showed the least mass gain, 0.14 ± 0.004 mg/cm^2, after 500 h. Despite having similar compositions, AISI 444 showed a much lower net mass gain than AISI 441 (almost half) after 500 h, indicating slower oxidation kinetics in AISI 444. The net mass gain of AISI 444 and AISI 441 after 500 h were 0.43 ± 0.041 mg/cm^2 and
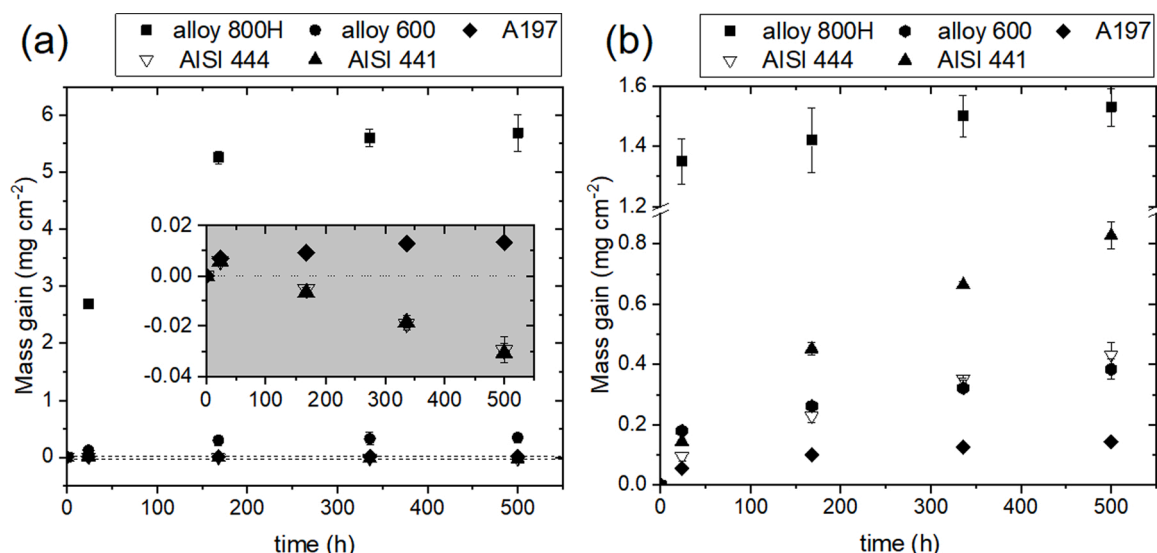

Fig. 1. Net mass gain as a function of time for the selected alloys exposed to (a) 650 °C and (b) 850 °C in air + 3 % H_2O for 500 h.

0.82 ± 0.045 mg/cm^2, respectively.

3.2. Chromium evaporation

Fig. 2a, b show the data from the time-resolved chromium evaporation measurements conducted on the five selected alloys at 650 °C and 850 °C, respectively. Alloy 800H, which showed a high mass gain at 650 °C, showed very low chromium evaporation. Alloy 600 showed a five times higher chromium evaporation than alloy 800H. A197 showed the least chromium evaporation of all the alloys at 650 °C. AISI 444 and 441, which showed a net mass loss at 650 °C, showed the highest chromium evaporation of the selected alloys; the chromium evaporation from AISI 441 was slightly higher than from AISI 444. The chromium evaporation of the selected alloys was 2.5–4 times higher at 850 °C than at 650 °C, except for alloy 800H, which had a 10 times higher chromium evaporation at 850 °C. However, the ranking of materials according to chromium evaporation was the same at both temperatures. The increase in chromium evaporation with temperature is in line with Opila et al. [43], who have demonstrated that the equilibrium constant, K_p, of Eq. (1), is higher at higher temperatures, indicating that the equilibrium pressure of $CrO_2(OH)_2$ increases with temperature. The mass gain of the coupons used for chromium evaporation is measured after 500 h and matches well with the mass gain measurements from the discontinuous exposures.

3.3. Microstructural investigation

3.3.1. Oxide scale at 650 °C

The broad ion beam milled SEM micrographs in the cross-sections of the alloys exposed for 500 h at 650 °C is shown in Fig. 3. All the alloys showed a continuous oxide scale with no signs of spallation. The cross-section micrograph of alloy 800H is shown in Fig. 3a. The cross-section micrograph shows that the oxide scale was continuous and non-uniform with outward- and inward-growing parts. The thickness of the oxide scale was not uniform, varying from 15 to 70 μm. EDX maps of the marked area are shown in Fig. 5a. They revealed that the oxide scale comprises three distinct layers (labelled 1, 2, and 3 in Fig. 3a). The top layer of the oxide scale was enriched in iron, Fe_2O_3 (confirmed with XRD), growing outwards. Underneath the Fe_2O_3, the layer was rich in Fe and Ni oxide (label 2 in Fig. 3a). Discontinuous patches of aggregated Ni-rich oxide, NiO (confirmed with XRD), were visible at the original interface of the alloy, separating outward- and inward-growing parts. Under the original interface, an inward-growing intermediate oxide layer (label 3 in Fig. 3a) rich in iron, chromium and nickel is observed. The concentration of the chromium increased towards the metal-oxide interface. The oxide scale was dominant in chromium at the metal-oxide interface. The lack of a continuous protective oxide throughout the scale led to breakaway corrosion; however, the oxide scale healed by forming a protective Cr-rich scale at the metal-oxide interface, which resulted in a sharp drop in the oxidation rate.

The cross-section and surface morphology (insert) of alloy 600 is shown in Fig. 3b. The cross-section revealed that the oxide scale was non-uniform across the surface with two types of oxide scale: a thick non-protective oxide scale and a thin protective oxide scale. The thick oxide scale was multi-layered with varying thickness. The oxide scale grew both inwards (crater) and outwards (islands) in these regions. The outward-growing islands were either isolated or semi-continuous, spread all over the surface, and were of various sizes (1 μm –10 μm). Fig. 5c shows the EDX maps of the oxide scale in cross-section. EDX maps revealed that the islands and craters had varying local enrichments in the regions with a thicker oxide scale. The islands were rich in Fe and Ni, composed of two layers; the top layer was rich in Ni (NiO), and an intermediate oxide layer featured local enrichments of Cr, Fe, and Ni. The crater was composed of an intermediate oxide layer rich in Ni, Cr ($NiCr_2O_4$). The XRD analysis shown in Fig. 6b confirms the presence of NiO and $NiCr_2O_4$. The oxide scale was depleted of chromium in the islands but was rich in the craters. Chromium enrichment was also visible at the metal-oxide interface in the crater. The absence of internal oxidation in the thinner oxide regions indicates a protective oxide scale that was too thin to be resolved in an EDX. A similar scale was found on Ni-20Cr thin foils exposed to air at 500 °C. A TEM investigation showed that the oxide scale had an outer NiO and an inner chromia scale [44]. The protective scale is speculated to have been formed due to an enhanced chromium supply related to local defects in the region.

The cross-section of A197 in Fig. 3c indicates the formation of a continuous protective oxide scale with no signs of spallation. The scale was uniform, with a thickness of about 50 nm after 500 h. Reactive element oxides were sometimes seen in the oxide scale. A more detailed analysis was not possible because the oxide scale was very thin. Nevertheless, based on the mass gain and chromium evaporation data, it can be concluded that the oxide scale on A197 is superior to chromia scale [40].

The cross-section of AISI 444 in Fig. 3d shows a thin oxide layer with a thickness of around 200 nm. EDX analysis (Appendix Fig. A.1a) revealed a continuous $(Cr,Fe)_2O_3$ scale with a discontinuous $(Cr,Mn)_3O_4$ spinel on the surface. The XRD shown in Fig. 6a supports the EDX analysis, indicating the presence of $(Fe,Cr)_2O_3$ and $(Cr,Mn)_3O_4$. Laves phase precipitates $(FeCrSi)_2(MoNb)$ were visible in the alloy matrix, at grain boundaries, and at the metal-oxide interface. The cross-section of AISI 441 in Fig. 3e shows a slightly thicker oxide scale (about 300 nm)
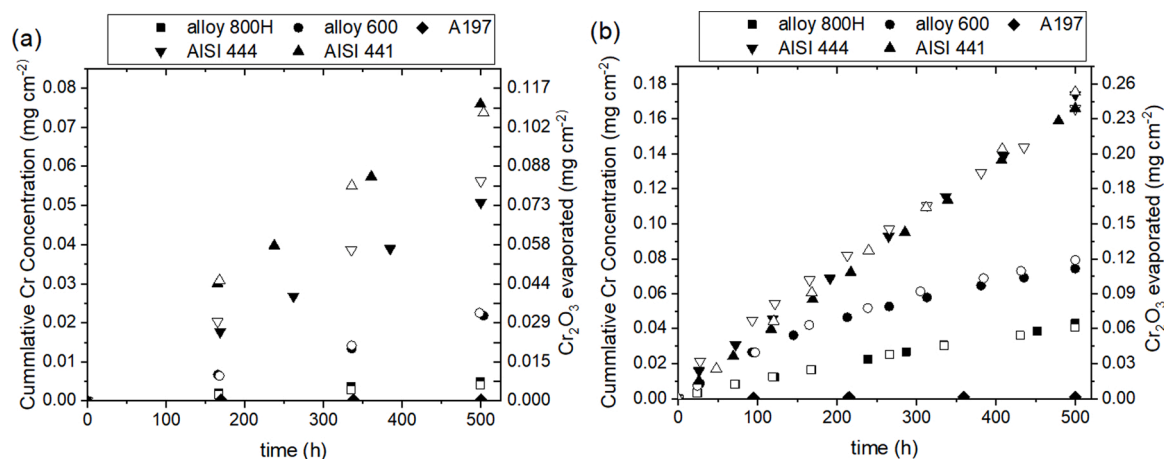

Fig. 2. Cumulative chromium evaporation as a function of time for the selected alloys exposed to (a) 650 °C and (b) 850 °C in air + 3 % H_2O for 500 h. Open and filled symbols represent two individual exposures.
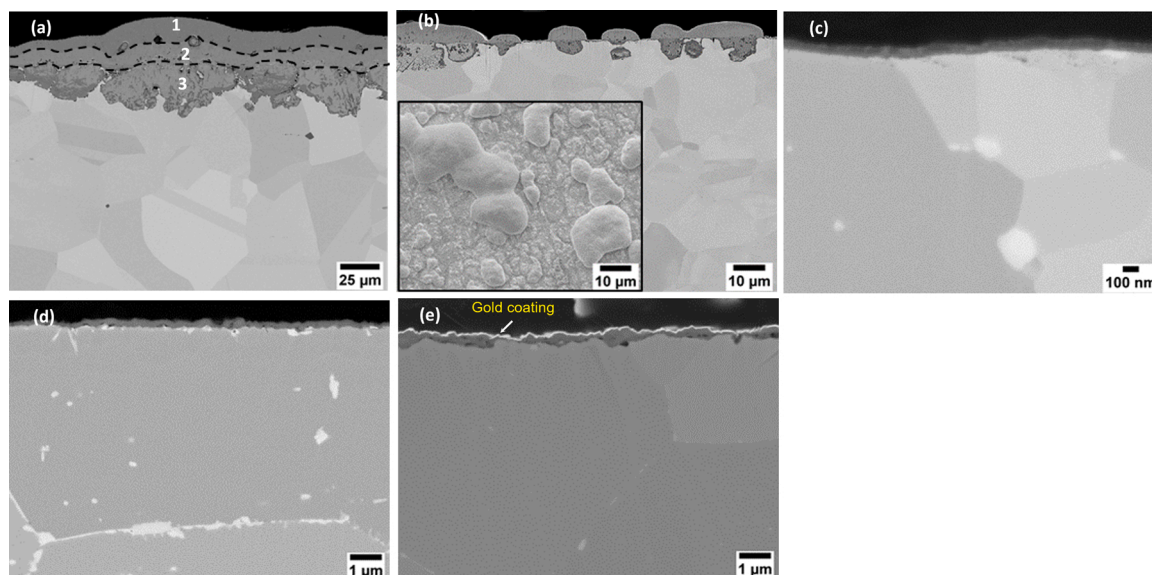
Fig. 3. SEM cross-section micrographs of (a) Alloy 800H (b) Alloy 600 (c) A197 (d) AISI 444 (e) AISI 441 exposed 650 °C in air + 3 % H$_2$O for 500 h.

than AISI 444. Nevertheless, the structure and composition of the oxide scales in these alloys was quite similar. XRD measurements (Fig. 6a) showed the presence of (Fe,Cr)$_2$O$_3$ and (Cr,Mn)$_3$O$_4$ on the surface. Laves phase precipitates were visible primarily along the grain boundaries. The laves phases had a lower volume fraction in AISI 441 than in AISI 444. This can be explained by lower combined mole fraction of Nb and Mo in AISI 441 [45].

3.3.2. Oxide scale at 850 °C

Fig. 4 shows the broad ion beam milled cross-sections of the alloys exposed for 500 h at 850 °C. The cross-section of alloy 800H in Fig. 4a shows that the oxide scale at 850 °C was similar to the scale at 650 °C; the oxide scale structure was different above the alloy grains compared to the oxide scale structure in the vicinity of alloy grain boundaries, and the oxide layer consisted of inward-growing and outward-growing parts with one major difference; the oxide scale was much thinner at 850 °C than at 650 °C, as reflected in mass gain. Fig. 5b shows the EDX maps of the alloy exposed for 500 h. The top layer of the oxide scale was rich in

Ni and Fe (Fe,Ni)$_3$O$_4$ spinel (confirmed with XRD), and it was free of chromium (within the detection limit of the EDX). No Fe$_2$O$_3$ or NiO enrichments were visible as they were at 650 °C. A continuous Cr-rich oxide scale was visible at the metal-oxide interface. There was an intermediate oxide layer composition enriched with Ni, Fe, and Cr between the top spinel layer and the Cr-rich oxide layer, but only above the alloy grains. Such a layer was absent close to the alloy grain boundaries. Internal oxidation of aluminium and titanium was visible primarily along the grain boundaries.

The SEM cross-sectional image of alloy 600 (Fig. 5b) revealed that the oxide scale was non-uniform and multi-layered. Fig. 5d shows the EDX elemental maps of the oxide scale. The oxide scale was thinner around the alloy grain boundaries and thicker above the alloy grain. These results are in agreement with Xiao et al. [46] for alloy 600 and Calvarin et al. [44] for Ni-20Cr foil at high temperatures. The oxide scale above the alloy grains was thicker and multi-layered, featuring a nickel-rich phase at the oxide-air interface. Underneath the top layer was an intermediate region of the oxide scale composed of Ni and Fe
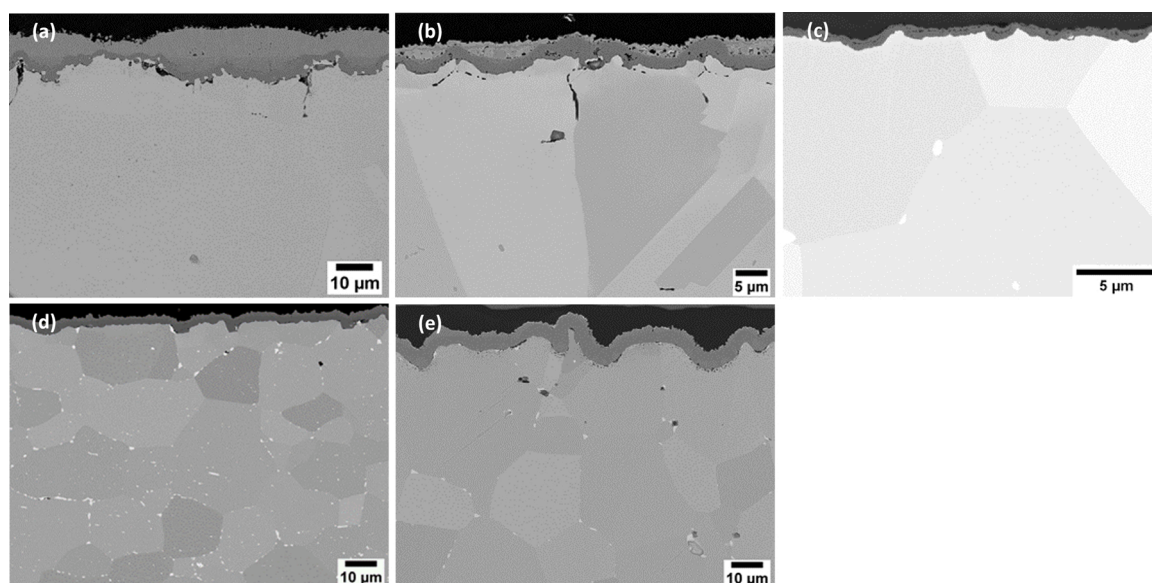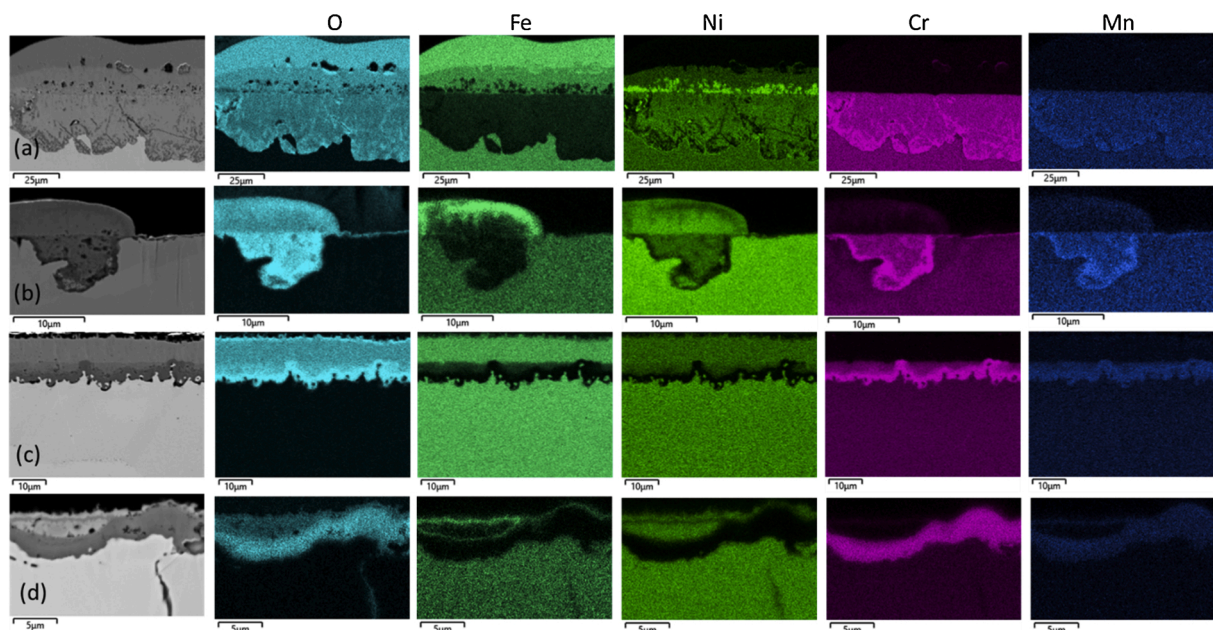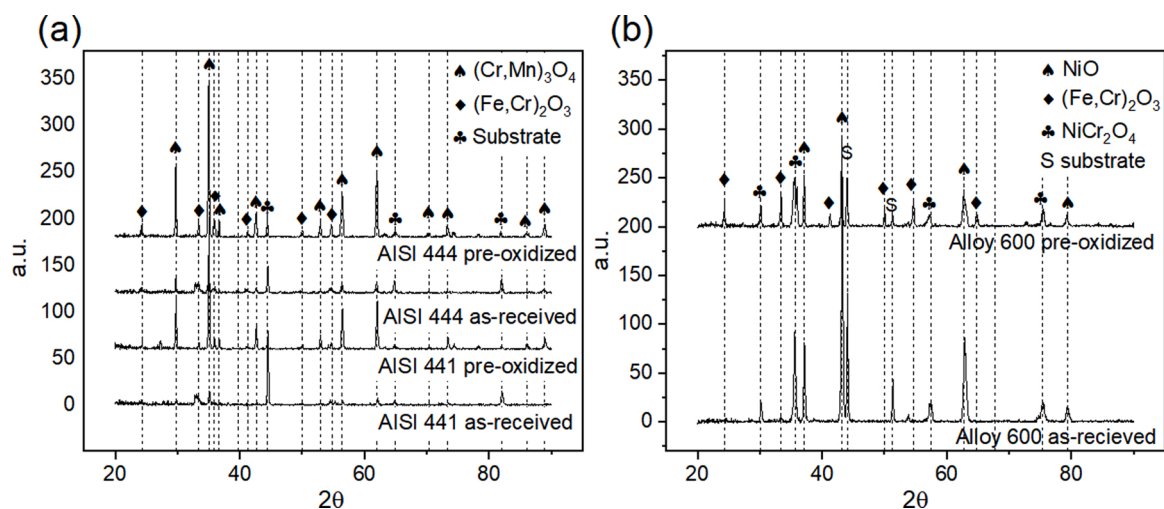

Fig. 4. SEM cross-section micrographs of (a) Alloy 800H (b) Alloy 600 (c) A197 (d) AISI 444 (e) AISI 441 exposed 850 °C in air + 3 % H$_2$O for 500 h.

Fig. 5. EDX maps of O, Fe, Ni, Cr, Mn in cross-section of Alloy 800H at 650 °C (a), 850 °C (b) and Alloy 600 at 650 °C (c), 850 °C (d) exposed in air + 3 % H_2O for 500 h. (colour).

Fig. 6. (a) XRD analysis of AISI 441 and AISI 444 in as-received and pre-oxidized conditions exposed at 650 °C for 500 h. (b) XRD analysis of alloy 600 in as-received and pre-oxidized conditions exposed at 650 °C in air + 3 % H_2O for 500 h.

with a varying composition featuring local enrichments. A chromia scale was visible in the inner part, next to the metal-oxide interface. In contrast, the oxide scale near the alloy grain boundaries had a nickel-rich top oxide scale, which was thin. An intermediate layer was absent in these regions. A continuous chromia layer was found underneath the poor top layer.

The cross-section of A197 in Fig. 4c indicates the formation of a continuous alumina scale with no signs of spallation. The scale was uniform, with a scale thickness of around 500 nm. The oxide scale was comprised of a dense inner layer, while the outer layer was porous towards the metal-air interface. Sand et al. [47] have investigated an A197 oxide scale with STEM in humid environments at 800 °C and reported that the outer scale was rich in Si, while the inner scale was rich in Al after 200 h. Sand et al. [47] have also reported the presence of mullite ($Al_2(Al_{2+2x}Si_{2-2x})O_{10-x}$) and tridymite ($SiO_2$ polymorph) in addition to α-alumina and γ-alumina, using XRD. Reactive elements oxides were sometimes seen in the oxide scale, and the oxide scale was thicker in

those locations.

The SEM cross-sectional image of AISI 444 in 4d shows a continuous double-layered oxide. EDX analysis (Appendix Fig. A.2a) revealed that the thin top of the oxide layer was rich in Mn and Cr, a $(Cr,Mn)_3O_4$ spinel and had a thick inner oxide, Cr_2O_3. The oxide layer was uniform, with a thickness of 2−3 μm. Laves phase precipitates were visible in the alloy grains, and the alloy grain boundaries, however, coarser than the laves phase precipitates observed at 650 °C. The SEM cross-sectional image of AISI 441 in 4e shows a wavy oxide with two distinctive layers. The oxide scale structure is similar to the one of AISI 444, with an outer $(Cr,Mn)_3O_4$ spinel and an inner Cr_2O_3 scale. However, the oxide scale was thicker than that of AISI 444 - with a thickness of 3−4 μm - which was also reflected in the net mass gain (Fig. 1b). A zone of internal titanium oxidation was visible under the metal-oxide interface. Unlike at 650 °C, laves phase precipitates were visible only along the grain boundaries.

3.4. Effect of pre-oxidation

Fig. 7a and b show the data for net mass gain and chromium evaporation, respectively, for the coupons pre-oxidized at 900 °C in laboratory air for 24 h and subsequently exposed to air with 3% H_2O for 500 h at 650 °C. The mass gain of the selected alloys upon pre-oxidation (Table 2) at 900 °C was similar to the net mass gains when exposed to air + 3 % H_2O at 850 °C for 24 h, only slightly higher. An exception was alloy 800H, where the net mass gain decreased with increasing exposure temperature.

The net mass gain of pre-oxidized coupons on exposure at 650 °C were very low for alloy 800H and A197, and the net mass gain was negative for alloy 600, AISI 444, and AISI 441. The most striking difference was found for the pre-oxidized alloy 800H, which showed a net mass gain of 0.043 ± 0.06 mg cm^{-2} (excluding the mass gain in pre-oxidation: 0.73 mg cm^{-2}), whereas the as-received coupon showed 5.69 ± 0.31 mg cm^{-2}. Pre-oxidized alloy 600 exposed for 500 h at 650 °C showed a net mass loss compared to the as-received coupons, which showed a significant net mass gain. Pre-oxidized A197 showed a negligible change in mass after exposure, indicating a highly protective oxide scale. Pre-oxidized AISI 444 and AISI 441 showed a net mass loss similar to the as-received coupons. The pre-oxidized coupons showed a slightly higher net mass loss than the as-received coupons.

The pre-oxidized alloy 800H and A197 had low chromium evaporation similar to the respective as-received coupons. Chromium evaporation decreased from 30 to 50 % for the pre-oxidized coupons compared to the as-received ones for alloy 600, AISI 444, and AISI 441. Nevertheless, at 650 °C, the ranking of the materials concerning chromium evaporation was similar in pre-oxidized and as-received coupons. The pre-oxidized samples had oxide scales identical to the as-received ones exposed at 850 °C. When further exposed at 650 °C, the pre-oxidized chromia-forming alloys had 7–10 times lower chromium evaporation than the as-received ones exposed at 850 °C. This agrees with Falk-Windisch et al. [40], who have reported that chromium evaporation increases by 2−3 times per 100 °C on chromia-forming alloys in the studied temperature range.

4. Discussion

4.1. Corrected mass gain

The net mass gain values plotted in Fig. 1 do not directly correlate to the oxide formed by the reaction between metal and oxygen. Chromium evaporation affects the net mass gain; thus, it is misleading the extent of oxidation and Cr consumption in the alloy. Hence, for a rational comparison, one needs to compensate net mass gain with the material lost to

Table 2
Net mass gains of the selected alloys after 24 h exposed to different conditions.

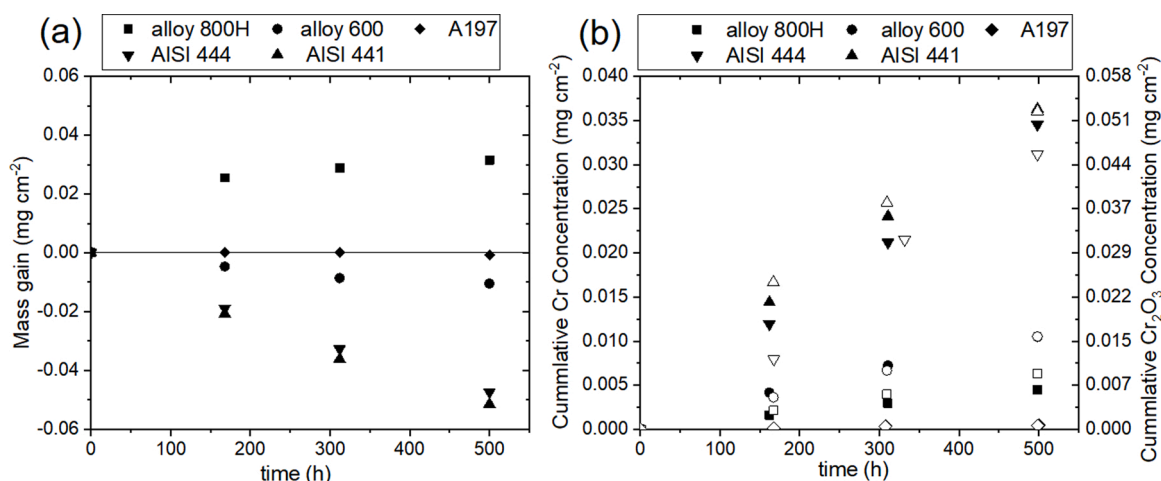| Material	850 °C air + 3 % H_2O	900 °C in air
Alloy 800H	1.35	7.03E-01
Alloy 600	1.80E-01	2.33E-01
A197	5.43E-02	7.84E-02
AISI 444	9.39E-02	2.17E-01
AISI 441	1.44E-01	3.18E-01

chromium evaporation to understand the true extent of oxidation, referred to as corrected mass gain. Spallation influences net mass gain, too; nevertheless, no spallation was observed during the experiments.

Table 3 shows the net mass gain and the corrected mass gain of the alloys at 650 °C and 850 °C, respectively. The mass of the evaporated chromia scale can be calculated from the evaporation data shown in Fig. 2. Eq. 1 shows the transformation of Cr_2O_3 to $CrO_2(OH)_2$; it has been estimated that 1 mg of Cr collected equals 1.46 mg of Cr_2O_3 lost from the oxide scale.

4.2. Alloy 800H

Despite having the highest Cr content of the investigated alloys, alloy 800H exhibited the highest mass gain under all exposure conditions. The performance of alloy 800H was especially poor at 650 °C without pre-oxidation. This can be explained by the slow Cr diffusion in austenitic steels such as alloy 800H [48]. The lack of a protective Cr-rich oxide layer led to the formation of fast-growing oxides that grew both outwards and inwards, resulting in a high mass gain. In the initial stage, a fast-growing iron-rich oxide scale formed on the surface through outward diffusion. This led to the high mass gain observed in the first 24 h. It is not before a thick oxide is formed that a Cr rich layer can be established at the metal-oxide interface.

The diffusion of Cr is substantially faster at higher temperatures, leading to the faster formation of a Cr-rich protective scale at 850 °C. Hence, an inverse temperature behaviour was observed with lower mass gain at higher temperatures. Nevertheless, the oxide-air interface was composed of Ni and Fe oxides. The higher temperature resulted in a faster solid-state reaction between Fe_2O_3 and NiO, resulting in (Fe, Ni)$_3O_4$ spinel (confirmed with XRD). An intermediate oxide layer rich in Ni, Cr, and Fe was present mostly above the alloy grains due to slower chromium diffusion through bulk than along the grain boundaries [49], which also act as preferential nucleation sites for the Cr-rich oxide scale [44]. The oxidation of Ni, Cr, and Fe during the transient stage occurred mostly above the alloy grains, and the oxidation was subsequently stopped by the formation of a Cr-rich protective scale through lateral

Fig. 7. (a) Net mass gain (b) Cumulative chromium evaporation of the pre-oxidized samples exposed 650 °C in air + 3 % H_2O for 500 h.

Table 3
Net and corrected mass gains of the selected alloys after 500 h at 650 °C and 850 °C in air with 3 %H$_2$O.

Material	650 °C (as-recieved)		650 °C (pre-oxidized)		850 °C	
	Net mass Gain (mg/cm^2)	Corrected mass Gain (mg/cm^2)	Net mass Gain (mg/cm^2)	Corrected mass Gain (mg/cm^2)	Net mass Gain (mg/cm^2)	Corrected mass Gain (mg/cm^2)
Alloy 800H	5.6934	5.7004	0.036	0.04	1.5295	1.5924
Alloy 600	0.3429	0.3758	−0.011	0.005	0.3839	0.4997
A197	0.0134	0.0139	0.001	0.0011	0.1422	0.1445
AISI 444	−0.0295	0.0526	−0.048	0.0015	0.4316	0.6417
AISI 441	−0.0307	0.0769	−0.0515	0.0025	0.8275	1.0764

and bulk diffusion.

The oxide scale microstructure of alloy 800H upon pre-oxidation at 900 °C was similar to the microstructure at 850 °C. However, the outer Ni-Fe oxide layer was thinner at 900 °C as the protective, Cr-rich oxide scale formed much faster at higher temperatures. This resulted in the low mass gain observed in the subsequent exposure at 650 °C. After 24 h at 850 °C and 900 °C, most of the surface of alloy 800H was covered with a Fe- and Ni-rich oxide, while a small fraction of the surface was covered with chromia as the outermost layer. Nevertheless, these regions disappeared, and only the Fe- and Ni-rich oxide was visible on the surface after continued exposures. Chen et al. [50] and Khalid et al. [51] have found that the Cr-rich scale of alloy 800H becomes dominant when ground alloy 800H is exposed to air at 950 °C and 1000 °C.

The chromium evaporation of alloy 800H was significantly lower than the chromium evaporation of the chromia-forming ferritic steels in the study. Chromium evaporation levels similar to those for Co-coated ferritic steels [15] were reached for alloy 800H without the need for coatings. The low chromium evaporation was due to a thick oxide layer at 650 °C and a Ni-Fe spinel oxide cap layer at 850 °C on the chromia scale. Ni-Fe coatings have been reported to suppress the growth of chromia and inhibit the outward diffusion of chromium [7]. Thus, the Ni-Fe oxide cap layer increased the lifespan of alloy 800H by suppressing the growth of the chromia layer and the depletion of chromium through evaporation, which usually triggers breakaway corrosion. In contrast, similar alloys that cannot form an oxide cap layer such as, Sanrico 25 [52], AISI 310 [53,54], AISI 304 [42,55,56], have been reported to suffer local and/or complete breakaway corrosion when exposed to an O$_2$ + H$_2$O environment at 600 °C – 800 °C due to chromium evaporation. The Fe- and Ni-rich cap layer effectively suppressed chromium evaporation, making alloy 800H attractive as a BOP component if a proper pre-oxidation step can be implemented.

4.3. Alloy 600

Despite the lower Cr content in alloy 600 (about 16 %) than in alloy 800H (20 %), the mass gain for alloy 600 was significantly lower than for alloy 800H at 650 °C. This was due to the oxide scale formed on alloy 600, which was partly a thin protective oxide scale but also contained a thick non-protective region. In contrast, Xiao et al. [46] have reported no protective chromia scale on alloy 600 polished to 2 μm exposed to similar conditions at 600 °C. The difference in the oxide scale can be attributed to the lack of surface defects on the polished sample [57]. At 850 °C, higher chromium diffusion through the bulk and the alloy grain boundaries was adequate to form a continuous chromia scale. Nevertheless, a thin layer of continuous NiO was visible at the air-oxide interface, and an intermediate oxide layer rich in Ni, Cr, and Fe was observed only above alloy grains on top of the chromia scale, similar to alloy 800H.

The lack of a continuous protective chromia scale at 650 °C led to the high net mass gain, similar to the net mass gain at 850 °C. There was also a substantial difference in the mass gain at 650 °C between the as-received and pre-oxidized coupons. This difference was due to a continuous protective chromium-rich oxide scale on the pre-oxidized

coupons. The chromium evaporation of the pre-oxidized coupons was about 50 % lower than the as-received ones. This difference was likely due to the thicker Ni-rich cap layer formed upon pre-oxidation. The presence of NiO and the mixed oxide layer above the chromia scale limits chromia access to the environment. Nevertheless, chromium evaporation was higher for alloy 600 than for alloy 800H due to a thinner and inferior cap layer.

4.4. A197

Alumina is known for its excellent chromium retention capabilities. A197, FeCrAl alloy, showed the least chromium evaporation of all the steels at both exposure temperatures. The chromium evaporation of A197 was about two orders of magnitude lower than the chromia-forming ferritic steels at the exposed temperatures. The thickness of the oxide scales for A197 after 500 h at 650 °C and 850 °C was about 50 nm and 500 nm, respectively, indicating the high oxidation resistance of the alloy. Alumina-forming alloys are known for their high oxidation resistance; however, they are dependent on the formation of α-alumina, which is typically formed at high temperatures. Nevertheless, A197 showed the formation of a slow-growing protective scale at much lower temperatures. The cumulative chromium evaporation at 650 °C on the as-received coupons and the pre-oxidized coupons was similar and was extremely low. The oxide scale formed at 650 °C proved to be superior to chromia scales.

4.5. AISI 441 & AISI 444

Chromia-forming ferritic steels, AISI 441 and AISI 444, had similar oxide scale structures, an outer Cr-Mn spinel and an inner Cr$_2$O$_3$ scale, when exposed to 850 °C and pre-oxidized at 900 °C. The oxide scale of these alloys was also similar at 650 °C. Compared to 850 °C, the oxide scale is thinner, and the outer Cr-Mn spinel was found in discontinuous patches.

The net mass gain behaviour of these alloys was similar at 650 °C, regardless of the pre-treatment conditions; they showed mass loss with time. Chromium evaporation was similar for both alloys in all exposure and pre-treatment conditions. However, the chromium evaporation of the pre-oxidized coupons was lower than the as-received coupons at 650 °C. The formation of a continuous Cr-Mn spinel on the pre-oxidized coupons resulted in lower chromium evaporation. (Cr,Mn)$_3$O$_4$ spinel is known to decrease chromium evaporation by 60–70 % compared to the Cr$_2$O$_3$ scale at 800 °C [31]. The corrected mass gain for the pre-oxidized coupons was lower than the as-received, indicating an improvement in oxidation behaviour upon pre-oxidation.

In contrast, the mass gain behaviour for these alloys was different at 850 °C. AISI 441 showed a higher net and corrected mass gain than AISI 444 at 850 °C and upon pre-oxidation. These results corroborate the findings of earlier studies on these alloys [19,20]; however, the reasons are not completely understood. It is speculated that Mo addition affects the defect structure of chromia [58] and the higher volume fraction of laves phases in AISI 444 [19] influences the oxidation rate. However, such variations in oxidation are not found at lower temperatures due to

slower oxidation kinetics. Despite differences in oxide scale thickness at 850 °C, chromium evaporation was similar for these alloys because of their similar $(Cr,Mn)_3O_4$ spinel cap layers. Overall, the chromium evaporation of these alloys was very high, making them unsuitable for BOP components.

To summarize the austenitic materials, alloy 800H and alloy 600, showed higher net mass gain than the other selected alloys at 650 °C due to the lack of a protective oxide scale. The ferritic steels, AISI 444, AISI 441, and A197, formed a protective scale, resulting in a low net mass gain. The chromium evaporation of AISI 441 and AISI 444 was higher than the chromium evaporation of austenitic materials due to the higher Cr content in the outer oxide scales of the former. At 650 °C, FeCrAl alloy, A197 performed the best while the other alloys behaved poorly either in terms of chromium evaporation or oxidation behaviour. Pre-oxidation significantly improved the performance of the alloys, alloy 800H in particular. Pre-oxidation of alloy 800H helped to form a continuous chromia layer resulting in a low mass gain.

Mass gain and chromium evaporation were higher for the selected alloys at 850 °C than at 650 °C. Alloy 800H had very low chromium evaporation due to the formation of a protective Ni-Fe spinel on the top of the chromia layer. Similarly, alloy 600 had a discontinuous and thin NiO cap layer, which reduced chromium evaporation, but the chromium evaporation was still higher than alloy 800H. The highest chromium evaporation was recorded for AISI 441 and AISI 444. A197 had the lowest mass gain and chromium evaporation of the selected alloys.

5. Conclusions

- Cr, Al-lean FeCrAl alloy, A197 had the lowest mass gain and chromium evaporation at the exposed temperatures. The chromium evaporation of A197 was approximately two orders of magnitude lower than the chromium evaporation of AISI 441 and AISI 444 at both exposure temperatures.
- Alloy 800H formed a fast-growing oxide, which makes it a poor choice, particularly at 650 °C. Nevertheless, alloy 800H was characterized by very low Cr evaporation, a highly desirable property for SOFC application. Pre-oxidized alloy 800H combined these properties: low oxidation rate and very low Cr-evaporation rate.
- Of the investigated alloys, alloy 600 showed an intermediate performance: it exhibited significant chromium evaporation and oxide scale growth. Although better than AISI 441 and 444, it was inferior to pre-oxidized 800H and A197. Considering the high cost of the material, alloy 600 is predicted to be a poor choice for BOP components.
- AISI 441 and AISI 444 had a similar mass gain at 650 °C, but AISI 444 showed lower mass gain than AISI 441 at 850 °C. Chromium evaporation was similar for both the materials and is the highest of the selected alloys at the exposed temperatures. High mass gain and high chromium evaporation make these materials unsuitable for BOP components.

Data availability

The raw/processed data required to reproduce these findings will be made available on request.

CRediT authorship contribution statement

Mareddy Jayanth Reddy: Conceptualization, Investigation, Writing - original draft, Writing - review & editing. **Jan-Erik Svensson:** Conceptualization, Writing - review & editing, Supervision, Funding acquisition. **Jan Froitzheim:** Conceptualization, Writing - review & editing, Funding acquisition, Supervision, Project administration.

Declaration of Competing Interest

The authors declare that they have no known competing financial interests or personal relationships that could have appeared to influence the work reported in this paper.

Acknowledgements

Appendix A. Supplementary data

Supplementary material related to this article can be found, in the online version, at doi:https://doi.org/10.1016/j.corsci.2021.109671.

References

[1] A. Buonomano, F. Calise, M.D. d'Accadia, A. Palombo, M. Vicidomini, Hybrid solid oxide fuel cells-gas turbine systems for combined heat and power: a review, Appl. Energy 156 (2015) 32–85, https://doi.org/10.1016/j.apenergy.2015.06.027.

[2] A. Choudhury, H. Chandra, A. Arora, Application of solid oxide fuel cell technology for power generation - A review, Renew. Sustain. Energ. Rev. 20 (2013) 430–442, https://doi.org/10.1016/j.rser.2012.11.031.

[3] Y. Kobayashi, K. Tomida, M. Nishiura, K. Hiwatashi, H. Kishizawa, K. Takenobu, Development of Next-generation Large-scale SOFC Toward Realization of a Hydrogen Society, 2015. https://power.mhi.com/randd/technical-review/pdf/index_01e.pdf.

[4] S.P. Jiang, X. Chen, Chromium deposition and poisoning of cathodes of solid oxide fuel cells - A review, Int. J. Hydrogen Energy 39 (2014) 505–531, https://doi.org/10.1016/j.ijhydene.2013.10.042.

[5] B. Talic, V. Canovic, M. Nikumaa, P.V. Hendriksen, R. Kiebach, Comparison of MnCo2O4 coated Crofer 22 H, 441, 430 as interconnects for intermediate-temperature solid oxide fuel cell stacks, J. Alloys. Compd. 821 (2020), https://doi.org/10.1016/j.jallcom.2019.153229.

[6] J. Froitzheim, S. Canovic, M. Nikumaa, R. Sachitanand, L.G. Johansson, J. E. Svensson, Long term study of Cr evaporation and high temperature corrosion behaviour of Co coated ferritic steel for solid oxide fuel cell interconnects, J. Power Sources 220 (2012) 217–227, https://doi.org/10.1016/j.jpowsour.2012.06.092.

[7] Q. Zhao, S. Geng, G. Chen, F. Wang, Initial oxidation behavior of ferritic stainless steel interconnect with sputtered NiFe2 alloy coating, Oxid. Met. 93 (2020) 283–299, https://doi.org/10.1007/s11085-019-09954-6.

[8] Manufacturing Cost Analysis of 1, 5, 10 and 25 kW Fuel Cell Systems for Primary Power and Combined Heat and Power Applications, 2017. https://www.energy.gov/sites/prod/files/2018/02/f49/fcto_battelle_mfg_cost_analysis_1%20_to_25kw_pp_chp_fc_systems_jan2017_0.pdf.

[9] J.L. Córdova, H. Heshmat, Development of a Ceramic Heat Exchanger for Application As Solid Oxide Fuel Cell Cathode Air Preheater, 2016, https://doi.org/10.1115/POWER2016-59333.

[10] J.A. Schuler, Z. Wuillemin, A. Hessler-Wyser, C. Comminges, N.Y. Steiner, J. Van herle, Cr-poisoning in (La,Sr)(Co,Fe)O3 cathodes after 10,000h SOFC stack testing, J. Power Sources 211 (2012) 177–183, https://doi.org/10.1016/j.jpowsour.2012.03.045.

[11] A.N. Aphale, L. Ravi Narayan, B. Hu, A. Pandey, P. Singh, Surface pretreatment of alumina forming alloy and its implication on Cr evaporation, ECS Trans. 85 (2018) 57–63, https://doi.org/10.1149/08502.0057ecst.

[12] S. Bhowmick, G. Le, A. Verma, P. Singh, Assessment of Chromium Evaporation From Chromia and Alumina Forming Alloys, John Wiley & Sons, Ltd, 2011, pp. 115–124, https://doi.org/10.1002/9781118095249.ch10.

[13] K. Zhang, A. El-Kharouf, J.-E. Hong, R. Steinberger-Wilckens, The effect of aluminium addition on the high-temperature oxidation behaviour and Cr evaporation of aluminised and alumina-forming alloys for SOFC cathode air pre-heaters, Corros. Sci. 169 (2020), 108612, https://doi.org/10.1016/j.corsci.2020.108612.

[14] S. Chevalier, L. Combemale, I. Popa, S. Chandra-ambhorn, W. Chandra-ambhorn, P. Promdirek, P. Wongpromrat, Chapter 6 development of SOFC interconnect stainless steels, Solid State Phenom. 300 (2020) 135–156, https://doi.org/10.4028/www.scientific.net/SSP.300.135.

[15] J.G. Grolig, J. Froitzheim, J.E. Svensson, Coated stainless steel 441 as interconnect material for solid oxide fuel cells: oxidation performance and chromium evaporation, J. Power Sources 248 (2014) 1007–1013, https://doi.org/10.1016/j.jpowsour.2013.08.089.

[16] R. Trebbels, IEF-2, Reduktion der Chromfreisetzung aus metallischen Interkonnektoren für Hochtemperaturbrennstoffzellen durch Schutzschichtsysteme, RWTH Aachen, 2009. https://juser.fz-juelich.de/record/5439.

[17] P. Piccardo, S. Anelli, V. Bongiorno, R. Spotorno, L. Repetto, P. Girardon, K44M ferritic stainless steel as possible interconnect material for SOFC stack operating at

600 °c: Characterization of the oxidation behaviour at early working stages, Int. J. Hydrogen Energy 40 (2015) 3726–3738, https://doi.org/10.1016/j.ijhydene.2015.01.083.

[18] V. Bongiorno, P. Piccardo, S. Anelli, R. Spotorno, Influence of surface finishing on high-temperature oxidation of AISI type 444 ferritic stainless steel used in SOFC stacks, Acta Metall. Sin. (English Lett. 30 (2017) 697–711, https://doi.org/10.1007/s40195-017-0543-1.

[19] J. Shu, H. Bi, X. Li, Z. Xu, The effects of molybdenum addition on high temperature oxidation behavior at 1,000 °c of type 444 ferritic stainless steel, Oxid. Met. 78 (2012) 253–267, https://doi.org/10.1007/s11085-012-9304-8.

[20] L. Faivre, P.O. Santacreu, A. Acher, A new ferritic stainless steel with improved thermo-mechanical fatigue resistance for exhaust parts. Mater. High Temp., Taylor & Francis, 2013, pp. 36–42, https://doi.org/10.3184/096034013X13637176323444.

[21] T. Manninen, J. Säynäjäkangas, Mechanical properties of ferritic stainless steels at elevated temperature, Proc. Fourth Int. Expert. Semin. Stainl. Steel Struct. (2012). http://www.steel-stainless.org/media/1124/32_manninen_t.pdf.

[22] L. Tan, T.R. Allen, Y. Yang, Corrosion behavior of alloy 800H (Fe-21Cr-32Ni) in supercritical water, Corros. Sci. 53 (2011) 703–711, https://doi.org/10.1016/j.corsci.2010.10.021.

[23] G. Hayner, R. Bratton, R. Wright, Next Generation Nuclear Plant Materials Research and Development Program Plan, 2005 (accessed April 9, 2020), https://www.osti.gov/biblio/911784.

[24] G.Y. Lai, High-Temperature Corrosion and Materials Applications, 2007 (accessed April 25, 2020), www.asminternational.org.

[25] H.M. Tawancy, On the comparative degradation of selected Cr2O3-forming alloys by high-temperature carburization with a case study involving 310 stainless steel, Eng. Fail. Anal. 110 (2020), 104402, https://doi.org/10.1016/j.engfailanal.2020.104402.

[26] R.C. Reed, The Superalloys, Cambridge University Press, Cambridge, 2006, https://doi.org/10.1017/CBO9780511541285.

[27] A.M. de Sousa Malafaia, R.B. de Oliveira, L. Latu-Romain, Y. Wouters, R. Baldan, Isothermal oxidation of Inconel 625 superalloy at 800 and 1000 °C: microstructure and oxide layer characterization, Mater. Charact. 161 (2020), 110160, https://doi.org/10.1016/j.matchar.2020.110160.

[28] A. Khanna, Introduction to High Temperature Oxidation and Corrosion, ASM International, 2003.

[29] Special Metals, INCONEL ® Alloy 600, 2008.

[30] T.S. Chester, N.S. Stoloff, W.C. Hagel, Superalloys II: High-Temperature Materials for Aerospace and Industrial Power, 2nd ed., Wiley Interscience, 1987.

[31] M. Stanislowski, J. Froitzheim, L. Niewolak, W.J. Quadakkers, K. Hilpert, T. Markus, L. Singheiser, Reduction of chromium vaporization from SOFC interconnects by highly effective coatings, J. Power Sources 164 (2007) 578–589, https://doi.org/10.1016/j.jpowsour.2006.08.013.

[32] F.G. Wilson, B.R. Knott, C.D. Desforges, Preparation and properties of some ODS Fe-Cr-Al alloys, Metall. Trans. A. 9 (1978) 275–282, https://doi.org/10.1007/BF02646711.

[33] R. Prescott, M.J. Graham, The formation of aluminum oxide scales on high-temperature alloys, Oxid. Met. 38 (1992) 233–254, https://doi.org/10.1007/BF00666913.

[34] W.S. Spear, D.H. Polonis, Interstitial precipitation in Fe-Cr-Al alloys, Metall. Mater. Trans. A. 25 (1994) 1135–1146, https://doi.org/10.1007/BF02652289.

[35] V. Asokan, J. Eklund, S. Bigdeli, T. Jonsson, The influence of Si on the primary protection of lean FeCrAl model alloys in O2 and O2+H2O at 600 °C—a microstructural investigation, Corros. Sci. 179 (2021), 109155, https://doi.org/10.1016/j.corsci.2020.109155.

[36] J. Eklund, B. Jönsson, A. Persdotter, J. Liske, J.E. Svensson, T. Jonsson, The influence of silicon on the corrosion properties of FeCrAl model alloys in oxidizing environments at 600 °C, Corros. Sci. 144 (2018) 266–276, https://doi.org/10.1016/j.corsci.2018.09.004.

[37] N. Israelsson, K. Hellström, J.-E. Svensson, L.-G. Johansson, KCl-induced corrosion of the FeCrAl alloy kanthal®AF at 600 °C and the effect of H2O, Oxid. Met. 83 (2015) 1–27, https://doi.org/10.1007/s11085-014-9506-3.

[38] J. Froitzheim, H. Ravash, E. Larsson, L.G. Johansson, J.E. Svensson, Investigation of chromium volatilization from FeCr interconnects by a denuder technique, J. Electrochem. Soc. 157 (2010) B1295, https://doi.org/10.1149/1.3462987.

[39] H. Falk-Windisch, J. Claquesin, M. Sattari, J.E. Svensson, J. Froitzheim, Co- and Ce/Co-coated ferritic stainless steel as interconnect material for intermediate

temperature solid oxide fuel cells, J. Power Sources 343 (2017) 1–10, https://doi.org/10.1016/j.jpowsour.2017.01.045.

[40] H. Falk-Windisch, J.E. Svensson, J. Froitzheim, The effect of temperature on chromium vaporization and oxide scale growth on interconnect steels for Solid Oxide Fuel Cells, J. Power Sources 287 (2015) 25–35, https://doi.org/10.1016/j.jpowsour.2015.04.040.

[41] B. Pujilaksono, T. Jonsson, M. Halvarsson, I. Panas, J.E. Svensson, L.G. Johansson, Paralinear oxidation of chromium in O 2 + H 2O environment at 600-700 °c, Oxid. Met. 70 (2008) 163–188, https://doi.org/10.1007/s11085-008-9114-1.

[42] H. Asteman, J.E. Svensson, M. Norell, L.G. Johansson, Influence of water vapor and flow rate on the high-temperature oxidation of 304L; effect of chromium oxide hydroxide evaporation, Oxid. Met. 54 (2000) 11–26, https://doi.org/10.1023/A:1004642310974.

[43] E.J. Opila, D.L. Myers, N.S. Jacobson, I.M.B. Nielsen, D.F. Johnson, J.K. Olminsky, M.D. Allendorf, Theoretical and Experimental Investigation of the Thermochemistry of CrO 2 (OH) 2 (g), J. Phys. Chem. A 111 (2007) 1971–1980, https://doi.org/10.1021/jp0647380.

[44] G. Calvarin, R. Molins, A.M. Huntz, Oxidation mechanism of Ni-20Cr foils and its relation to the oxide-scale microstructure, Oxid. Met. 53 (2000) 25–48, https://doi.org/10.1023/A:1004578513020.

[45] H. Ali-Löytty, M. Hannula, T. Juuti, Y. Niu, A.A. Zakharov, M. Valden, The role of (FeCrSi)2(MoNb)-type laves phase on the formation of Mn-rich protective oxide scale on ferritic stainless steel, Corros. Sci. 132 (2018) 214–222, https://doi.org/10.1016/j.corsci.2017.12.026.

[46] J. Xiao, N. Prud'Homme, N. Li, V. Ji, Influence of humidity on high temperature oxidation of Inconel 600 alloy: oxide layers and residual stress study, Appl. Surf. Sci. 284 (2013) 446–452, https://doi.org/10.1016/j.apsusc.2013.07.117.

[47] T. Sand, A. Edgren, C. Geers, V. Asokan, J. Eklund, T. Helander, J.E. Svensson, L. G. Johansson, Exploring the effect of Silicon on the high temperature corrosion of lean FeCrAl alloys in humid air, Oxid. Met. (2021), https://doi.org/10.1007/s11085-020-10019-2.

[48] T.M. Devine, Kinetics of sensitization and de-sensitization of duplex 308 stainless steel, Acta Metall. 36 (1988) 1491–1501, https://doi.org/10.1016/0001-6160(88)90216-7.

[49] X. Wang, J.A. Szpunar, Effects of grain sizes on the oxidation behavior of Ni-based alloy 230 and N, J. Alloys. Compd. 752 (2018) 40–52, https://doi.org/10.1016/j.jallcom.2018.04.173.

[50] W.S. Chen, W. Kai, L.W. Tsay, J.J. Kai, The oxidation behavior of three different zones of welded Incoloy 800H alloy, Nucl. Eng. Des. 272 (2014) 92–98, https://doi.org/10.1016/j.nucengdes.2014.01.022.

[51] F.A. Khalid, N. Hussain, K.A. Shahid, Microstructure and morphology of high temperature oxidation in superalloys, Mater. Sci. Eng. A 265 (1999) 87–94, https://doi.org/10.1016/S0921-5093(98)01181-2.

[52] L. Intiso, L.-G. Johansson, J.-E. Svensson, M. Halvarsson, Oxidation of Sanicro 25 (42Fe22Cr25NiWCuNbN) in O2 and O2 + H2O Environments at 600–750 °C, Oxid. Met. 83 (2015) 367–391, https://doi.org/10.1007/s11085-015-9528-5.

[53] H. Asteman, J.E. Svensson, L.G. Johansson, Oxidation of 310 steel in H2O/O2 mixtures at 600 °C: the effect of water-vapour-enhanced chromium evaporation, Corros. Sci. 44 (2002) 2635–2649, https://doi.org/10.1016/S0010-938X(02)00056-2.

[54] J.E. Tang, F. Liu, H. Asteman, J.-E. Svensson, L.-G. Johansson, M. Halvarsson, Investigation of FIB-thinned TEM cross-sections of oxide scales formed on type 310 steel at 600°C in water vapour-containing oxygen atmospheres, Mater. High Temp. 24 (2007) 27–55, https://doi.org/10.1179/096034007X207636.

[55] H. Asteman, J.E. Svensson, L.G. Johansson, M. Norell, Indication of chromium oxide hydroxide evaporation during oxidation of 304L at 873 K in the presence of 10% water vapor, Oxid. Met. 52 (1999) 95–111, https://doi.org/10.1023/A:1018875024306.

[56] H. Asteman, J.E. Svensson, L.G. Johansson, Evidence for chromium evaporation influencing the oxidation of 304L: the effect of temperature and flow rate, Oxid. Met. 57 (2002) 193–216, https://doi.org/10.1023/A:1014877600235.

[57] W.J. Nowak, B. Wierzba, Effect of surface treatment on high-temperature oxidation behavior of IN 713C, J. Mater. Eng. Perform. 27 (2018) 5280–5290, https://doi.org/10.1007/s11665-018-3621-2.

[58] M.F. Montemor, A.m.p. Simões, M.G.S. Ferreira, M.D.C. Belo, The role of Mo in the chemical composition and semiconductive behaviour of oxide films formed on stainless steels, Corros. Sci. 41 (1999) 17–34, https://doi.org/10.1016/S0010-938X(98)00126-7.